Green Chemistry

Accepted Manuscript

ROYAL SOCIETY OF CHEMISTRY

www.rsc.org/greenchem

Green Chemistry

ARTICLE

Ni Nanoparticles Encapsulated into Mesoporous Single-Crystalline HBEA: Application for Drainage Oil Hydrodeoxygenation to Diesel

Received 00th xx 2015,
Accepted 00th xx 2015

DOI: 10.1039/x0xx00000x

www.rsc.org/

Bing Ma, Jiangbo Hu, Yimeng Wang, Chen Zhao*[a]

To construct supported metal catalysts with high dispersion at high metal loadings is of crucial importance. The great challenge for achieving this goal lays on two aspects, that is, the stability of the support material with high surface areas and abundant mesopores at working conditions, as well as the metal nanoparticles agglomeration upon harsh treatments, especially for transition metals that are difficult to be reduced and easy to aggregate. To overcome these problems, here we propose a new and promising strategy for encapsulating the Ni nanoclusters (d = 5.6 nm) into/onto the uniform and inter-connected intra-mesopores (7-8 nm) of single-crystalline HBEA, achieving highly dispersive Ni nanoparticles (content: 40 wt %, dispersion: 3.5 %) on the stable carrier. The architecture of relative position of Ni nanoparticles and support is dedicatedly revealed by the direct proofs of ultrathin sections transmission electron microscope and N_2 sorption measurements, together with the indirect evidences of temperature programmed reduction of H_2 and IR spectroscopy of adsorbed CO. In comparison to such advantageous structure of metal to support, the Ni nanoparticles are commonly deposited on the limited external surface or inter-mesopores of the commercial HBEA carriers. Besides, the novel catalyst shows superior adsorption performance towards the large molecule. As expected, such catalyst leads to a significantly high initial rate of 132 mmol·g^{-1}·h^{-1} (equivalent to 38 g·g^{-1}·h^{-1}) and highly selective octadecane formation (96 % yield) from stearic acid conversion. Consequently, the high activity and stable durability are realized for four recycling runs of drainage oil hydrodeoxygenation with the newly developed Ni/HBEA.

Introduction

Drainage oil mainly includes waste animal and vegetable oil, swill oil, and garbage oil from sewer. [1] The production of drainage oil is enormous worldwide, especially in Asian countries such as in China. But the introduced salts and acids impurities as well as the diverse sources of drainage oil lead to components complicated, and thus, the further utilization of drainage oil becomes to be difficult. [2]

Currently, the main technique for drainage oil transformation uses the transesterification approach to produce biodiesel, that is, fatty acid mono-alkyl esters (FAAE), but such esters face the problem of a relatively high oxygen content and poor flow property at low temperatures. [3] Alternatively, the hydrodeoxygenation (HDO) method is considered to be a more promising technique that directly converts of drainage oil to hydrocarbon diesel oil. The bifunctional metal/acid catalysts combined with Ni nanoclusters and acidic supports show high efficiency for HDO of lipids to hydrocarbons. [4-6] The active sites of Pd [7], W [8] and Mo [9] are able to hydrodeoxygenate of lipids as well, but the achieved rates are still very low and thus need to be highly enhanced. In comparison to the reduced metallic Ni catalysts, the representative sulfided CoMo and NiMo catalysts manifest considerable HDO ability on lipids as well [10, 11], but the products are mainly composed of straight *n*-alkanes and these formed alkanes are easily contaminated by organosulfur compounds. By contrast, the acidic sites on the bifunctional sulfur-free catalysts generate a high isomerization fraction of branched alkanes, guaranteeing the property of diesel oil with low melting point. The reduced base Ni catalysts are, therefore, advantageous for selectively removing of the oxygen in the lipids.

The problem for utilization of Ni-based catalyst replies on that, the Ni nanoclusters are inclined to agglomerate under severe synthesis and reaction conditions, especially when they are deposited on the external surface without any confinement or protection. The growth of Ni nanoparticles leads to low HDO activities in the fresh and used catalysts. With respect to this issue, in the former work we have provided a solution which locates the Ni nanoclusters onto the uniform inter-crystalline mesopore (25 nm) to limit Ni nanoparticle agglomeration and enhance the rate for palm oil HDO to 19 g·g^{-1}·h^{-1} [12]. For designing an endogenous strategy, in this contribution we encapsulate the Ni nanoclusters into/onto the uniform and interconnected intra-mesopores (7-8 nm) of single-crystalline HBEA to achieve an ultra-high activity and stability for one-pot HDO of drainage oil to diesel oil at moderate conditions, offering a green and prospect solution for waste resource utilization to valuable fuels.

Results and discussion

Comparison of three HBEA with different morphologies

In the present work, a mesoporous single-crystalline HBEA (B-MS), together with two HBEA with Si/Al_2 ratios of 20 and 26

[a] Shanghai Key Laboratory of Green Chemistry and Chemical Processes, School of Chemistry and Molecular Engineering, East China Normal University, Shanghai, 200062, China
E-mail: czhao@chem.ecnu.edu.cn (C. Zhao)
† Footnotes relating to the title and/or authors should appear here.
Electronic Supplementary Information (ESI) available: [details of any supplementary information available should be included here]. See DOI: 10.1039/x0xx00000x

Table 1. The physicochemical properties of three HBEA samples.

Zeolite HBEA	S_{meso} [$m^2 \cdot g^{-1}$] [a]	S_{micro} [$m^2 \cdot g^{-1}$] [a]	V_{meso} [$cm^3 \cdot g^{-1}$] [a]	V_{micro} [$cm^3 \cdot g^{-1}$] [a]	$S_{meso\text{-}Hg}$ [$m^2 \cdot g^{-1}$] [b]	$V_{meso\text{-}Hg}$ [$cm^3 \cdot g^{-1}$] [b]	Acid *conc.* (Py-IR) [mmol·g^{-1}]		Crystal Size (μm) [c]
							BAS	LAS	
MS	399	282	0.62	0.13	92.3	0.21	0.09	0.15	0.75
20	200	445	0.58	0.18	67.6	0.25	0.20	0.15	0.10
26	48	574	0.18	0.24	0.09	0.02	0.18	0.14	0.30

[a] Specific surface areas and pore volumes are determined by N_2 sorption at 77 K.
[b] Specific surface areas and pore volumes are counted by intruding Hg into mesopores (diameter: 4-50 nm).
[c] Crystal sizes are calculated by SEM images.

(commercial samples, annotated as respective B-20 and B-26) are selected for comparison and investigation. In the synthesis of the mesoporous single-crystalline HBEA (B-MS), the polymer poly-diallyl-dimethyl-ammonium chloride (PDADMA) was used as a dual-functional template,[13] where the quaternary ammonium group played as a structure-directing agent for forming the BEA structure and a disordered intra-mesopore creator after removing of the template.

The summarized data for the physicochemical and acid properties of three HBEA supports are compiled at Table 1. The X-ray diffraction (XRD) powder patterns of three HBEA samples showed the characteristic peaks of HBEA crystal at 7° and 23° for three samples (Fig. 1a). The acid sites were probed by IR spectroscopy of adsorbed pyridine (Fig. S1). The results revealed that the Brønsted acid site of B-MS was 0.09 mmol·g^{-1}, which was lower than that of B-20 (0.20 mmol·g^{-1}) and B-26 (0.18mmol·g^{-1}). The N_2 adsorption/desorption isotherms (Fig. 1b) showed that B-MS exhibited a characteristic type I and IV isotherms, and the H1-type hysteresis loop with the capillary condensation at the P/P_0 of 0.5-0.8 suggested that all the adjacent intra-mesopores were interconnected.[13] The B-MS sample had a high external surface area (399 $m^2 \cdot g^{-1}$). The relatively narrow size-distribution of the mesopores of B-MS appeared at around 7-8 nm (inset in Fig. 1b). By contrast, the pore size distributions of B-20 were mainly centred in the random wide range of 5-10 nm and 30-60 nm (inset in Fig. 1b), as the mesopores of B-20 were constructed by random accumulation of small particles (S_{meso}: 200 $m^2 \cdot g^{-1}$). The feature of type I isotherm on the B-26 did not show a hysteresis loop, indicating the absence of the meso-porosity (S_{meso}: 48 $m^2 \cdot g^{-1}$).

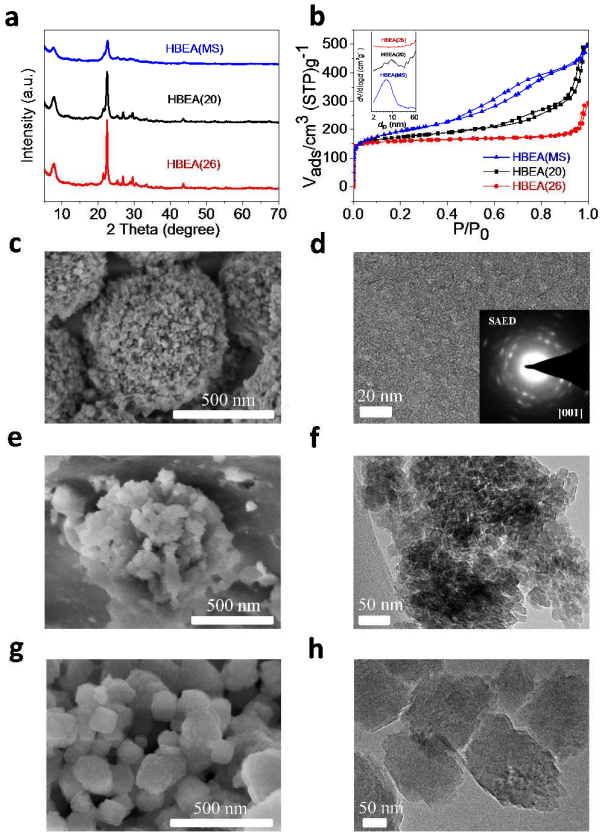

Figure 1. (a) XRD patterns and (b) N_2 adsorption and desorption isotherms of three HBEA samples, the inset shows the BJH adsorption pore size distributions. The SEM and TEM images of HBEA (MS), HBEA (20) and HBEA (26) were shown in the (c), (d), (e), (f), (g), and (h), respectively. The SAED pattern of HBEA was displayed in the inset of Fig. 1d.

Some distinct differences were observed between the structures of intra-mesopores in B-MS and inter-mesopores in B-20. The S_{meso} of B-MS (399 $m^2 \cdot g^{-1}$) was nearly two times higher than B-20 (S_{meso}: 200 $m^2 \cdot g^{-1}$), whereas the mesopore volumes of two samples were of small differences (0.62 vs 0.58 $cm^3 \cdot g^{-1}$) (Table 1). In an agreement, the method of mercury porosity (mercury is penetrated into 3-60 nm mesopores) showed that B-MS had an apparently larger S_{meso} (92.3 vs 67.6 $m^2 \cdot g^{-1}$) and a lower V_{meso} (0.21 vs 0.25 $cm^3 \cdot g^{-1}$) than B-20 (Table 1). This disparity is probably attributed to the fact that the mesopores at 5-60 nm (B-20) contribute to more inter-crystalline mesoporous volumes than those of B-MS when normalized to the zeolite weight.

The SEM image of B-MS (Figs. 1c and S2) showed that the single large and uniform crystals exhibited spherical shapes (sizes: 700-800 nm) with non-smooth surfaces, which were consisted of numbers of small crystals (approximate sizes: 3-4 nm). By contrast, B-26 (Figs. 1g and S2) displayed a regular round shape and a distinct particle size of 300 nm, while B-20 (Figs. 1e and S2) was consisted of sub-nano particles (50 nm) which were piped into an ordered flower shape with a crystal size of 1 μm (Table 1). The results of HRTEM images were perfectly fitted with those from HRSEM, that is, B-26 (Fig. 1h) was a bulky shape with a particle size of around 300 nm, while the particle size of B-20 was around 30-50 nm (Fig. 1f). The TEM image of B-MS indicated the consistent orientation lattice fringes over the entire images region (Fig. 1d), and furthermore, the selected area electron diffraction (SAED) (inset in Fig. 1d) demonstrated that the [001] direction exhibited discrete

diffraction spots rather than the diffraction halo, evidencing the single-crystalline nature of B-MS with small crystals (3-4 nm).

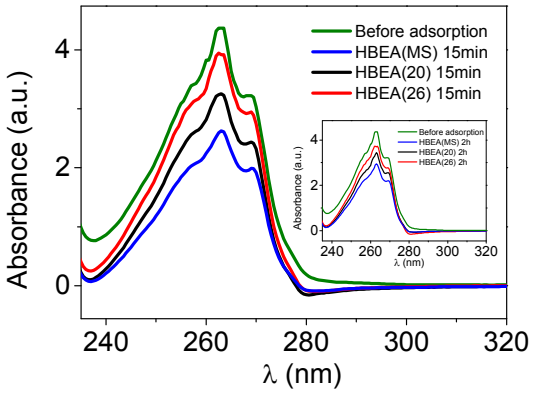

Figure 2. UV-vis spectra for the filtrate of the mixed TIPB and HBEA suspension in dodecane. Experiment: 1.0 g HBEA was added into 10 mL dodecane, and subsequently 0.0437 g TIPB was mixed with the formed suspension with stirring for 15 min. at ambient temperature. The centrifuged filtrate was detected by UV-vis detector.

To compare the adsorption performances of three HBEA samples, 1, 3, 5-triisopropylbenzene (TIPB) is used as a probe for UV-vis analysis (Fig. 2). TIPB was mixed with the HBEA sample in the dodecane solvent with stirring in a certain time at ambient temperature, and then the filtrate was analysed by UV-vis after centrifuging out of the solid. Compared to the solution before adsorption, the adsorption peak intensities (centered at 265 nm) were decreased after an adsorption time of 15 min. (Fig. 2), indicating that the TIPB concentration was decreased due to its adsorption on HBEA. After 2 h the peak intensity (after attaining equilibrium) followed the order $C_{B\text{-}26} > C_{B\text{-}20} > C_{B\text{-}MS}$ (Fig. 2 inset), suggesting that the TIPB adsorption rate and amount are fastest on B-MS. Since the diameter of TIPB (0.85 nm) [14] is larger than the pore diameter of HBEA (0.77 nm), the better adsorption performance of TIPB to HBEA is rationally attributed to the high external surface area of B-MS (399 $m^2 \cdot g^{-1}$). As compared to the commercial HBEA samples of B-20 and B-26 (Table 1), it can be concluded that B-MS has much higher external meso-porous surface area (399 $m^2 \cdot g^{-1}$) and more uniform interconnected intra-mesopore (V_{meso}: 0.62 $cm^3 \cdot g^{-1}$) at the centre pore sizes of 7-8 nm.

The architecture of Ni nanoparticles onto/into three HBEA carriers

Subsequently, the Ni nanoparticles were incorporated on the three HBEA zeolites by the deposition-precipitation method. The inductively coupled plasma (ICP) analysis indicated that B-MS was incorporated with much higher concentrations of Ni nanoclusters (40 wt% Ni loading) than B-20 (31 wt% Ni loading) and B-26 (29 wt% Ni loading) (Table 2). The Si content in Ni/B-20 sample (Si/Al = 11) was slightly lower than that in Ni/B-MS (Si/Al = 14) and Ni/B-26 (Si/Al = 14). The measurement of CO chemisorption demonstrated that three Ni/HBEA samples had almost comparable Ni dispersions at around 3% (see Table 2).

After incorporating Ni nanoparticles onto B-26, it was interesting to note that S_{meso} and V_{meso} of Ni/B-26 were sharply increased (Table S1, Fig. 4a), because the formed mesoporous Ni silicate sheet contributed to extra S_{meso} and V_{meso}. The HRSEM of

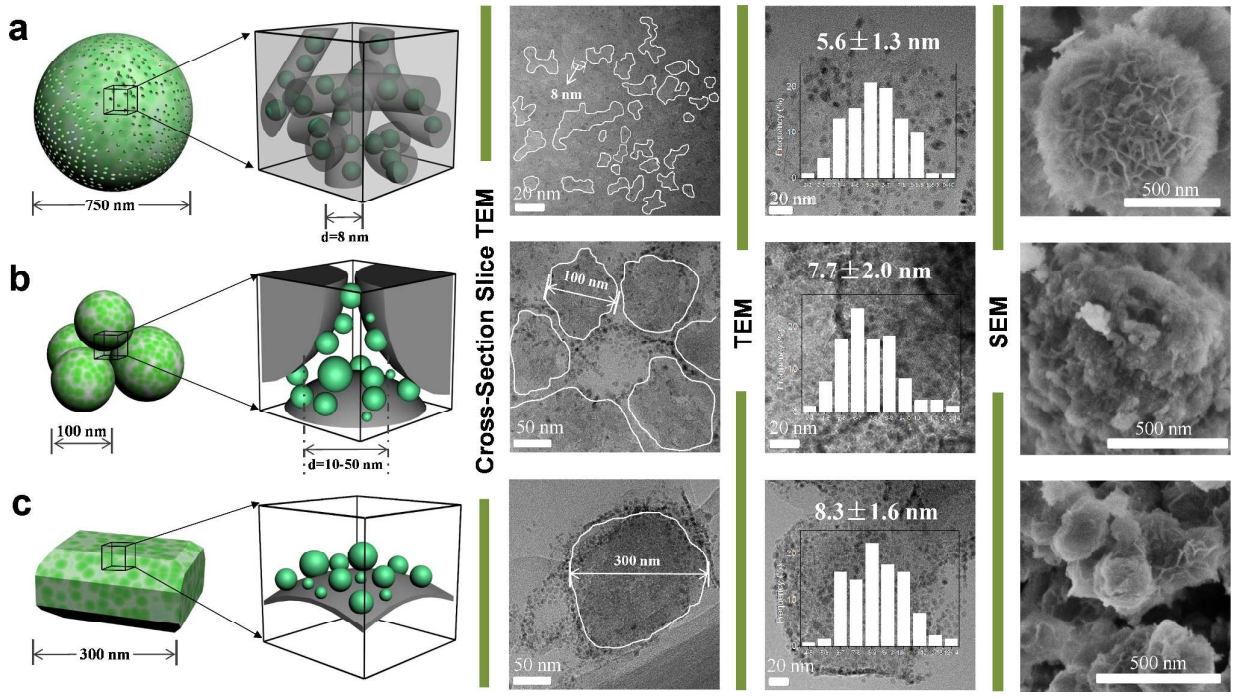

Figure 3. The distribution of Ni nanoparticles supported on (a) HBEA (MS), (b) HBEA (20), and (c) HBEA (26). The TEM and SEM images of Ni/HBEA (MS), Ni/HBEA (20), and Ni/HBEA (26) were shown on the right.

Table 2. The physicochemical, metallic, and acidic properties as well as activity tests on three Ni/HBEA samples.

Ni/HBEA	Si/Al [mol/mol] [a]	Metal loading [wt%] [a]	S_{meso} [$m^2 \cdot g^{-1}$] [b]	S_{micro} [$m^2 \cdot g^{-1}$] [b]	V_{meso} [$cm^3 \cdot g^{-1}$] [b]	V_{micro} [$cm^3 \cdot g^{-1}$] [b]	d_{Ni} [nm] [c]	D_{Ni} [%] [d]	Acid *conc.* (Py-IR) [mmol·g^{-1}]		Rate [$g \cdot g^{-1}_{Ni} \cdot h^{-1}$]	TOF [$mol \cdot mol^{-1}_{surf.\ Ni\ atom} \cdot h^{-1}$]
									BAS	LAS		
MS	14	40	277	206	0.62	0.09	5.6±1.3	3.5	0.02	0.25	38	778
20	11	31	172	365	0.59	0.16	7.7±2.0	3.4	0.15	0.42	13	336
26	14	29	126	383	0.31	0.17	8.3±1.6	3.2	0.11	0.33	11	317

[a] Analysed by ICP.

[b] Specific surface areas and pore volumes are determined by N_2 sorption at 77 K.

[c] Determined by TEM images.

[d] Calculated by CO chemisorption.

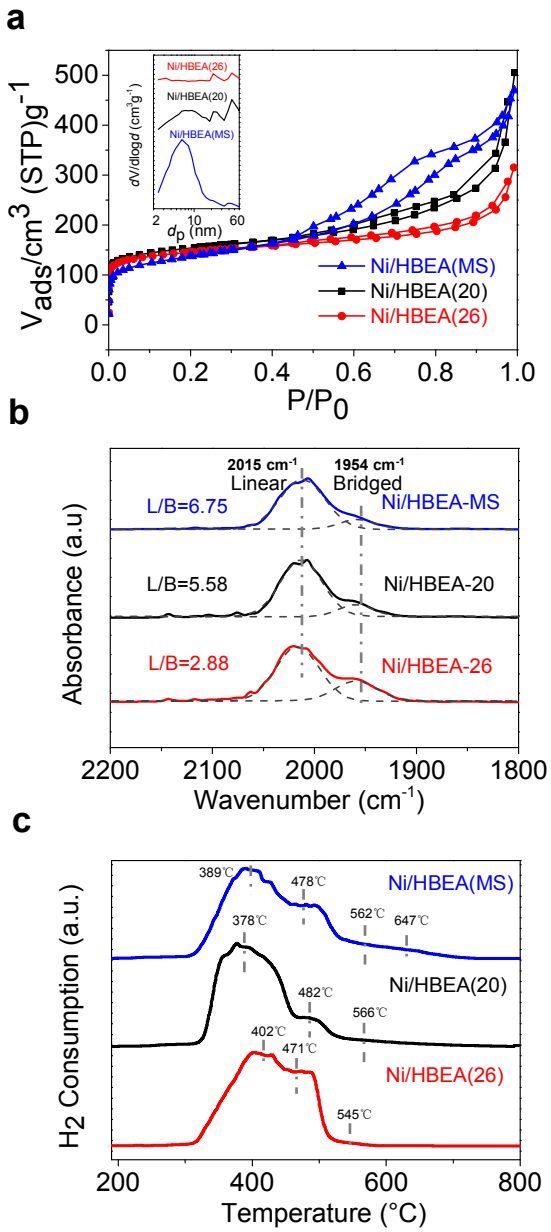

Figure 4. (a) The N_2 adsorption and desorption isotherms, the inset show the BJH adsorption pore size distributions, (b) the curve of IR spectra of adsorbed CO, (c) the profile of temperature programmed reduction of H_2 towards three Ni/HBEA catalysts.

Ni/B-26 (Figs. 3c and S3) confirmed the existence of Ni silicate phase [15, 16]. However, on the contrary the parameters of S_{meso} and V_{meso} of Ni/B-MS and Ni/B-20 were decreased compared to the parent supports. This may be due to the fact that the formed Ni particles entered into the mesopores of B-MS and B-20, and thus lowering the mesoporous volumes and external surface areas. In addition, the mesopore size of Ni/B-MS was shrunk from 8.0 nm (parent support) to 6.3 nm (Figs. 1b and 4a), which can indirectly certify that the Ni nanoparticles are encapsulated into mesoporous of Ni/B-MS and Ni/B-20. On the other hand, the obvious lowered Brønsted acid sites (parent: 0.09 mmol·g^{-1}) after Ni incorporation (Ni/B-MS: 0.02 mmol·g^{-1}) also suggest the Ni nanoclusters do enter into the pores of B-MS (Table 2).

In order to explore the relative position of Ni nanoparticles onto or into HBEA structure, three Ni/HBEA samples were cut into 30-50 nm slices by the method of ultrathin section. Shown from the TEM image (Fig. 3a), a thin slice from Ni/B-MS clearly evidenced that a number of Ni nanoparticles with size of 2-3 nm were located into the uniform intra-mesopores (d = 8 nm, Fig. 3a Cross-Section Slice TEM, the white circle). The average (external and internal) Ni nanoparticle sizes onto Ni/B-MS were around 5.6 ± 1.3 nm (Fig. 3a TEM), which were smaller than the intra-mesopore size of B-MS (around 8 nm). By contrast, the slice of Ni/B-20 from TEM image suggested that the Ni nanoparticles were supported on the interval spaces of accumulated HBEA particles (Fig. 3b, Cross-section slice TEM, the white circle). The Ni particle size was around 7.7 ± 2.0 nm when loaded onto the random inter-crystalline mesopores of B-20 (5-10 nm and 30-60 nm). For the B-26 support without mesopores, the Ni nanoparticles could be only supported onto the external surface of B-26 with the limited surface area (see Fig. 3c Cross-section slice TEM, the white circle), and the size of Ni nanoparticles on the outer surface of B-26 reached 8.3 ± 1.6 nm. The data of particle statistics demonstrated that the size of Ni nanoclusters of Ni/B-MS was smaller than the other two Ni catalysts, and this can be also confirmed by the information from XRD patterns (Fig. S4).

Based on the analysis of TEM, SEM, and N_2 sorption measurements, the architectures of Ni nanoparticles and HBEA support are displayed at Fig. 3. It can be deduced that for Ni/B-MS (crystal particle size: 750 nm), the Ni nanoparticles are loaded onto the outer surface as well as into the intra-crystalline pores of B-MS (d = 8 nm) (Fig. 3a, left). In comparison, for B-20 (crystal particle size: 100 nm) Ni nanoparticles are located on the mesopores of accumulated HBEA particles (d = 10-50 nm), as depicted in Figure 3b left. Compared to the hierarchical B-MS and B-20 samples, the micropore zeolite B-26 (crystal particle size: 300 nm) can only incorporate Ni on the limited outer surfaces. Through comparison, it can be deduced that the superior structure of B-MS can load more

accessible Ni nanoclusters onto/into the external surface and intra-crystalline uniform pores.

The Ni particles diameter statistics showed that the size of Ni particles followed the order $d_{Ni/B\text{-}MS} < d_{Ni/B\text{-}20} < d_{Ni/B\text{-}26}$, as determined from the TEM images (Figure 3). Such tendency is consistent with the data of IR spectra of adsorbed CO on three Ni catalysts (Fig. 4b). The adsorption of the linear and bridged CO species (denoted as L and B) correspond to IR bands at 2010-2070 cm^{-1} and 1930-1950 cm^{-1} [17-19]. Generally, the integrated IR intensity ratio of L to B (L/B) decreases when Ni particle size increases [20]. The calculated values of L/B were 6.75, 5.58 and 2.88 for Ni/B-MS, Ni/B-20, and Ni/B-26, respectively. The suggested smaller sizes of Ni/B-MS and Ni/B-20 from IR spectra imply that the growth of Ni particles is restricted by the intra- and inter-mesopores. The profile of temperature programmed reduction of H_2 demonstrates the different Ni species on the supports [21]. The reduction peaks at 380-480 °C and 540-560 °C are assigned to the respective NiO and surface nickel philosilicates species, while the peak at a high temperature of 647 °C of Ni/B-MS is attributed to the reduction of Ni species in the intra-mesopores [22]. The higher reduction temperature indicates a much stronger interaction of Ni nanoparticles with the HBEA support for the Ni/HBEA-MS catalyst.

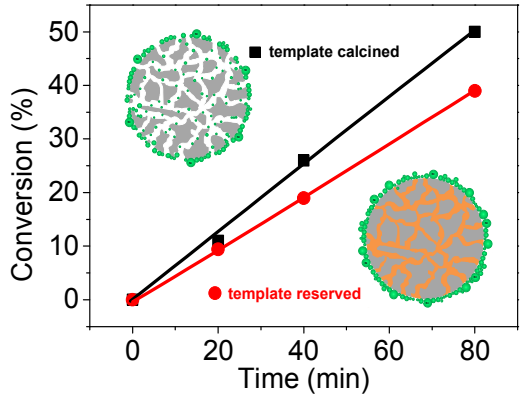

Figure 5. Comparison of stearic acid conversion over Ni/B-MS with and without template as a function of time. Reaction conditions: stearic acid (5.0 g), catalyst (0.2 g), dodecane (80 mL), 40 bar H_2, at a stirring speed of 600 rpm.

In order to illustrate the function of Ni particles in the intra-mesopores, we synthesized two kinds of Ni based samples: Ni nanoparticles that were incorporated into/onto the B-MS zeolites with and without inter-pores. The creation of inter-crystalline mesopores is manipulated by removing of the template by calcination at 550 °C (Fig. 5). The activities of these two types of Ni catalysts were then evaluated and compared in the reaction of stearic acid HDO (Fig. 5). The Ni/B-MS sample (with intra-crystalline mesopores) exhibited an obviously much higher activity at attaining a conversion at 50% after 80 min. than Ni/B-MS (without intra-crystalline mesopores) (conv: 39%) at identical condition. Meanwhile, the ICP result also indicated that the Ni content on the B-MS (with intra-crystalline mesopores: 11%) was higher than the other sample without intra-crystalline mesopores (Ni content: 9%). Through comparison, the enhanced activity is rationally attributed to the Ni nanoparticles encapsulated into the intra-mesopores.

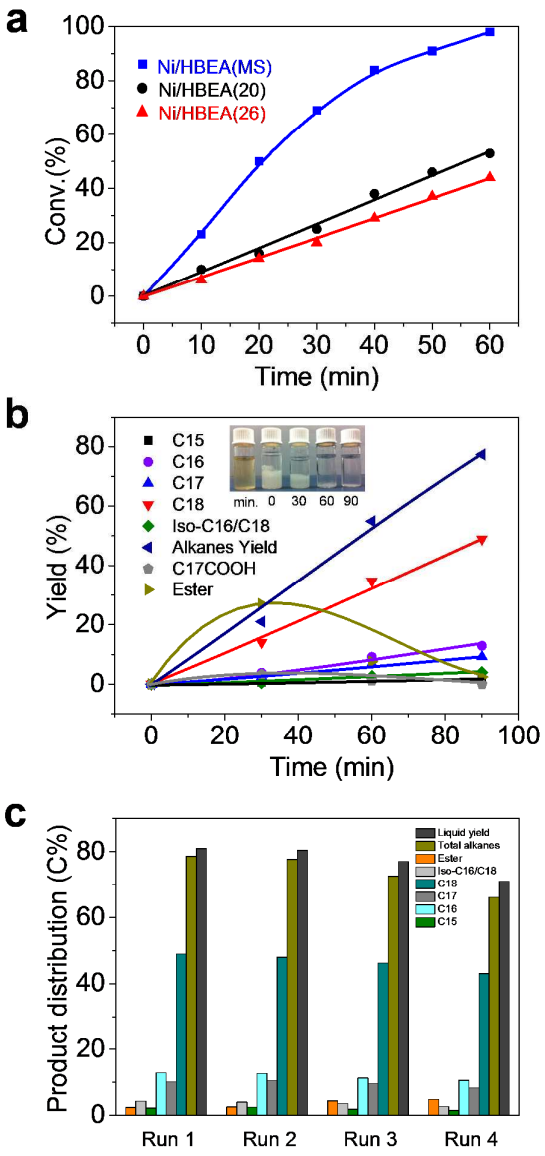

Figure 6. (a) The conversions of stearic acid with three Ni/HBEA catalysts as a function of time, (b) the kinetics of drainage oil hydrodeoxygenation over Ni/B-MS as a function of time, and (c) recycling tests of drainage oil hydrodeoxygenation over Ni/B-MS after 90 min.. General conditions: 5.0 g stearic acid, 0.2 g Ni/HBEA catalyst, or 5.0 g drainage oil, 0.8 g Ni/B-MS, 80 mL dodecane, 260 °C, 4 MPa H_2, stirring at 600 rpm.

Combing these results allows us to conclude that Ni/B-MS is supported with ultra-high concentrations of accessible Ni nanoparticles, and these uniform and interconnected intra-mesopores (7-8 nm) lead to the confined Ni particles (5.5 nm) equably distributed and are against nanoparticle agglomeration or growth to a large extent, which are beneficial for the further contact and transformation of fatty acids and triglyceride feedstock.

Evaluation of catalytic performances for stearic acid and drainage oil hydrodeoxygenation

The HDO measurements of model compound stearic acid and waste drainage oil were in turn evaluated in dodecane at 260 °C with 4 MPa H_2. The plotted kinetics curves for stearic acid conversion over three Ni/HBEA catalysts (Fig. 6a) with a fixed substrate and catalyst ratio of 25 $g{\cdot}g^{-1}$ demonstrated that a nearly complete conversion was obtained over Ni/B-MS after 1 h, whereas the conversions with Ni/B-20 and Ni/B-26 were only 53% and 44% at identical conditions, respectively (Table S2 and Fig. S5). The initial hydrodeoxygenation rates were decreased from 38 to 13, 11 $g{\cdot}g^{-1}{\cdot}h^{-1}$ accordingly (Table 2). If it is normalized to the accessible Ni atom on the surface, the obtained turnover frequencies (TOFs) were respective 778, 336, 317 $mol{\cdot}mol_{surf.\ Ni\ atom}^{-1}{\cdot}h^{-1}$. It indicated that Ni/B-MS performed remarkably superior to Ni/B-20 and Ni/B-26. It should be addressed that the activity of Ni/B-MS (attaining an initial rate: 38 $g{\cdot}g^{-1}{\cdot}h^{-1}$) is magnitudes higher than the previously reported catalysts, such as sulfided CoMo [23] (initial rate: 1.2 $g{\cdot}g^{-1}{\cdot}h^{-1}$ at 340-380 °C), Pd/C [24] (initial rate: 0.9 $g{\cdot}g^{-1}{\cdot}h^{-1}$ at 300 °C), the transition metals WO_3/WC_2 [8, 9] and Fe [25] catalysts (initial rate: 1.3 $g{\cdot}g^{-1}{\cdot}h^{-1}$ and 0.17 $g{\cdot}g^{-1}{\cdot}h^{-1}$), as well as common Ni/HBEA catalyst (initial rate: 5.0 $g{\cdot}g^{-1}{\cdot}h^{-1}$ at 260 °C) [5].

The highly enhanced catalytic activity on Ni/B-MS is mainly attributed to the highly accessible uniform Ni nanoclusters onto/into external surface and inter-crystalline pores of B-MS. Besides, the high rate can be also explained indirectly by the hierarchy factor (HF, defined as $S_{meso}{\times}V_{micro}/S_{total}/V_{total}$), which was proposed by Perez-Ramirez [26]. The HF for Ni/B-MS was 0.10, while such value for Ni/B-26 and of Ni/B-20 were 0.59 and 0.17, respectively, addressing the relatively high meso-porosity of B-MS. In addition, it was worthwhile to address that Ni/B-MS produced the highly selective octadecane (96% yield, see supporting information Table S2), suggesting that an atomic economic route of hydrogenation-dehydration is established for the involved overall HDO process.

The tests of stearic acid transformation clarify the advantageous ability of Ni/B-MS for HDO, and then it is applied for crude drainage oil HDO at identical conditions (260 °C, 4 MPa H_2). Drainage oil was received from Shanghai Lvming Environment Protection Technology Co., Ltd.. The used drainage oil had a pungent smell and a high acid and peroxide value, and its components of drainage oil were far more complicated than other types of pure lipids, which contained fatty acid glycerol ether polymers composing of unsaturated C_{18} fatty acids (72 %), saturated C_{18} fatty acids (5.8 %), saturated C_{16} fatty acids (18.8 %), and a small quantities of C_9, C_{12}, C_{14}, C_{15}, C_{17}, C_{20} and C_{22} fatty acids (3.4 %) (see Table S3). Shown from Fig. 6b, the plotted kinetics curve of drainage oil HDO demonstrated that the alkanes yield was increased gradually with C_{16} alkanes (12.9%) and C_{18} alkanes (49.0%) as the main products at 90 min., which are in line with the components of drainage oil. The route for decarbonylation of fatty alcohols took a minor part, generating the corresponding small amounts of C_{15} (2.2%) and C_{17} (10.2%) alkanes. The Brønsted acid sites of Ni/B-MS catalyzed the isomerization reaction of the formed alkenes and alkanes for yielding 4.3% iso-C_{16}/C_{18} alkanes. In the gas phase, the major products were CH_4 (80.2% selectivity) and C_3H_8 (17.6% selectivity) (see Fig. S6). Methane was formed by methanation of produced CO (via decarbonylation of fatty alcohol) and H_2, while propane was majorly produced by hydrogenolysis of C-O bonds of triglycerides. A very small amount of C_2H_6 (2.2% selectivity) was detected as well, which was probably derived from hydrogenolysis of glycol distearate in the crude drainage oil. These results imply that the occurrence of catalytic cracking of hydrocarbons is almost negligible. The hydrodeoxygenation reaction attained a rate of 3.4 $g_{oil}{\cdot}g_{cat.}^{-1}{\cdot}h^{-1}$, equivalents to TOF of 337 $g_{oil}{\cdot}g_{Ni\ surf.\ atom}^{-1}{\cdot}h^{-1}$. Besides, it also illuminated that the formed fatty acid and esters were initially increased to the maximum value and then gradually decreased, since the free fatty acids swiftly reacted with the produced intermediate fatty alcohols in the initial stage. The rate of esterification reaction was very fast under working conditions, as the observed ester intermediates were more abundant than fatty acids during the conversion. The in situ sampled products during drainage oil conversion were displayed at Fig. 6b inset. The diluted drainage oil in dodecane solvent showed a yellow color, and afterwards the formed esters and fatty acids (white solids) were the initial product from crude oil, and finally completely transformed to the final alkanes (transparent colorless liquid) after 90 min..

The stability of Ni/B-MS on converting of the drainage oil was tested in four consecutive recycling runs. In the recycling reactions, prior to use the catalyst was washed with acetone to remove the residual organics, and then subsequently air-calcined and hydrogen-reduced. The production distribution histogram was displayed at Fig. 6c, and in the first run it attained 81% liquid yield after 90 min., including 2.2% C_{15}, 12.9% C_{16}, 10.2% C_{17}, 49% C_{18} and 4.3% isomerized C_{16} and C_{18}, nearly approaching the theoretical yield (85 %). The liquid yield from drainage oil conversion still reached 71% in the fourth run, suggesting that Ni/B-MS possessed high catalyst durability. The slight deactivation of Ni/B-MS is probably attributed to small amounts of aggregated Ni nanoparticles on the external surface during the successive reactions. Such technique intrinsically realizes several separate processes including decolorization, deodorant, hydrodeoxygenation and isomerization into an integrated one-pot course, establishing a simple and efficient catalysis system for direct drainage oil utilization to valuable diesel oil.

Conclusions

In conclusion, we have designed a new bifunctional metal/zeolite catalyst by encapsulating Ni nanoparticles into/onto intra-mesopores of the single-crystalline HBEA for efficiently upgrading of crude drainage oil to diesel-ranged hydrocarbons in a one-pot process. The supported ultra-high accessible Ni nanoparticles into/onto the interconnected mesopores and external surface construct a promising HDO catalyst, bringing in super-fast rates for fatty acid and drainage oil HDO with better adsorption performance towards large molecules, as well as high catalyst stability via impeding nanoparticle agglomeration by pore confinement. The specific structure of Ni nanoparticles that are encapsulated into the intra-mesopores of single-crystalline HBEA offers more possibilities for application in shape-sensitive (to metal/acid sites) reactions.

Acknowledgements

This research was supported by the Recruitment Program of Global Young Experts in China and Shanghai Pujiang Program PJ1403500.

Notes and references

† Electronic Supplementary Information (ESI) available: [details of any supplementary information available should be included here]. See DOI: 10.1039/c000000x/

1 M. G. Kulkarni and A. K. Dalai, *Ind. Eng. Chem. Res.,* 2006, **45**, 2901–2913.
2 M. K. Lam, K. T. Lee and A. R. Mohamed, *Biotechnol. Adv.,* 2010, **28**, 500–518.
3 B. Peng, Y. Yao, C. Zhao and J. A. Lercher, *Angew. Chem. Int. Ed*., 2012, **51**, 2072–2075.
4 C. Zhao, T. Brück and J. A. Lercher, *Green Chem.,* 2013, **15**, 1720–1739.
5 W. Song, C. Zhao and J. A. Lercher, *Chem. Eur. J.,* 2013, **19**, 9833–9842.
6 C. V. Viêgas, I. Hachemi and D. Y. Murzin, et al. *Fuels,* 2015, **155**, 144–154.
7 K. Murata, Y. Liu, M. Inaba and I. Takahara, *Energy Fuels,* 2010, **24**, 2404–2409.
8 R. W. Gosselink, D. R. Stellwagen and J. H. Bitter, *Angew. Chem. Int. Ed.,* 2013, **125**, 5193–5196.
9 S. A. W. Hollak, R. W. Gosselink, D. S. van Es and J. H. Bitter, *ACS Catal.,* 2013, **3**, 2837–2844.
10 G. W. Huber, P. O. Connor and A. Corma, *Appl. Catal., A*, 2007, **329**, 120–129.
11 D. Kubička and L. Kaluža, *Appl. Catal. A,* 2010, **372**, 199–208.
12 B. Ma and C. Zhao, *Green Chem.,* 2015, **17**, 1692–1701.
13 J. Zhu, Y. Zhu, L. Zhu, M. Rigutto, A. van der Made, C. Yang, et al. *J. Am. Chem. Soc.,* 2014, **136**, 2503–2510.
14 N. Nishiyama, K. Ueyama and M. Matsukata, *J. Chem. Soc., Chem. Commun.,* 1995, 1967–1968.
15 J. van de Loosdrecht, A. M. van de Kraan, A. J. van Dillen and J. W. Geus, *J. Catal.,* 1997, **170**, 217–226.
16 M. Che, Z. Cheng and C. Louis, *J. Am. Chem. Soc.,* 1995, **117**, 2008–2018.
17 A. G. Sault, C. H. F. Peden and E. P. Boespflug, *J. Phys. Chem.,* 1994, **98**, 1652–1662.
18 J. Leglise, A. Janin, J. C. Lavalley and D. Cornet, *J. Catal.,* 1988, **114**, 388–397.
19 S. Derrouiche and D. Bianchi, *Appl. Catal. A* 2006, **313**, 208–217.
20 J. A. Anderson, M. T. Rodrigo, L. Daza and S. Mendioroz, *Langmuir*, 1993, **9**, 2485-2490.
21 M. V. Twigg and J. T. Richardson, *Appl. Catal. A,* 2000, **190**, 61–72.
22 K. Hadjiivanov, M. Mihaylov, D. Klissurski, P. Stefanov, N. Abadjieva, E. Vassileva and L. Mintchev, *J. Catal.,* 1999, **185**, 314–323.
23 R. Kumar, B. S. Rana, R. Tiwari, D. Verma, R. Kumar, R. K. Joshi, M. O. Garg and A. K. Sinha, *Green Chem*., 2010, **12**, 2232–2239.
24 J. G. Immer, M. J. Kelly and H. H. Lamb, *Appl. Catal., A,* 2010, **375**, 134–139.
25 K. Kandel, J. W. Anderegg, N. C. Nelson, U. Chaudhary and I. I. Slowing, *J. Catal.,* 2014, **314**, 142–148.
26 J. Pérez-Ramírez, D. Verboekend, A. Bonilla and S. Abelló, *Adv. Funct. Mater*., 2009, **19**, 3972–3979.

Table of Content: